Quaternary Research 81 (2014) 168–178

Contents lists available at ScienceDirect

Quaternary Research

journal homepage: www.elsevier.com/locate/yqres

^{10}Be exposure dating of river terraces at the southern mountain front of the Dzungarian Alatau (SE Kazakhstan) reveals rate of thrust faulting over the past ~400 ka

Anja Cording [a], Ralf Hetzel [a,*], Martin Kober [b], Jonas Kley [b,c]

[a] Institut für Geologie und Paläontologie, Westfälische Wilhelms-Universität Münster, Corrensstraße 24, 48149 Münster, Germany
[b] Institut für Geowissenschaften, Friedrich Schiller Universität Jena, Wöllnitzer Straße 7, 07749 Jena, Germany
[c] Now at: Geowissenschaftliches Zentrum, Georg-August-Universität Göttingen, Goldschmidtstraße 3, 37077 Göttingen, Germany

ARTICLE INFO

Article history:
Received 2 April 2013
Available online 21 November 2013

Keywords:
Active deformation
Thrust faulting
^{10}Be exposure dating
River terraces
Dzungarian Alatau
Tien Shan

ABSTRACT

The mountain belts of the Dzungarian Alatau (SE Kazakhstan) and the Tien Shan are part of the actively deforming India–Asia collision zone but how the strain is partitioned on individual faults remains poorly known. Here we use terrace mapping, topographic profiling, and ^{10}Be exposure dating to constrain the slip rate of the 160-km-long Usek thrust fault, which defines the southern front of the Dzungarian Alatau. In the eastern part of the fault, where the Usek River has formed five terraces (T_1–T_5), the Usek thrust fault has vertically displaced terrace T_4 by 132 ± 10 m. At two sites on T_4, exposure dating of boulders, amalgamated quartz pebbles, and sand from a depth profile yielded ^{10}Be ages of 366 ± 60 ka and 360 $^{+77}/_{-48}$ ka (both calculated for an erosion rate of 0.5 mm/ka). Combined with the vertical offset and a 45–70° dip of the Usek fault, these age constraints result in vertical and horizontal slip rates of ~0.4 and ~0.25 mm/a, respectively. These rates are below the current resolution of GPS measurements and highlight the importance of determining slip rates for individual faults by dating deformed landforms to resolve the pattern of strain distribution across intracontinental mountain belts.

Introduction

The Tien Shan is a 300–500 km wide intracontinental mountain belt in Central Asia that extends over a length of ~2000 km from Uzbekistan in the west to China in the east. In terms of geology and structure, the mountain ranges of the Boro Horo Shan and the Dzungarian Alatau are also part of the Tien Shan orogenic system (Fig. 1a). The Tien Shan system consists of generally east–west-trending mountain ranges with interspersed sedimentary basins and separates the Junggar basin and the Kazakh platform in the north from the Tarim basin in the south. The high topography of the Tien Shan, with summits exceeding 7000 m in elevation, resulted from the collision of India and possibly Arabia with Asia (e.g. Tapponnier and Molnar, 1979; Yin, 2010). Some authors attribute the location of the Tien Shan – far north of the locus of collision – to the reactivation of Paleozoic and/or Mesozoic basement structures (Windley et al., 1990; Hendrix et al., 1992; Jolivet et al., 2010). The initial uplift and exhumation during the Cenozoic was diachronous throughout the Tien Shan and started between the late Oligocene and the late Miocene in different parts of the mountain belt (e.g. Hendrix et al., 1994; Abdrakhmatov et al., 1996; Sobel and Dumitru, 1997; Yin et al., 1998; Bullen et al., 2001; Sobel et al., 2006; Charreau et al., 2009).

GPS studies show that the north–south shortening rate across the western Tien Shan is ~20 mm/a west of lake Issyk Kul (Fig. 1b) and decreases to ~9 mm/a over a distance of about 500 km toward the east (Reigber et al., 2001; Zubovich et al., 2010). The GPS studies also indicate that north–south contraction is not only focused along the edges of the orogen but also occurs in the interior of the mountain belt. Identifying and localizing the exact position of active faults, however, cannot be accomplished by GPS but requires detailed field investigations and mapping of landforms that are folded and/or tectonically offset by faults. If the age of such landforms (e.g. fluvial terraces, terrace risers, alluvial fans, and moraines) can be constrained via appropriate dating techniques such as radiocarbon, luminescence, or surface exposure dating, it is possible to quantify rates of faulting on time scales of 10^3 to 10^5 years. The determination of fault slip rates allows us to assess how active deformation is distributed across tectonically active mountain belts and has been increasingly applied to different portions of the India–Asia collision zone (e.g. Ritz et al., 2003; Hetzel et al., 2004; Kirby et al., 2007; Palumbo et al., 2009; Gold et al., 2011; Hetzel, 2013).

In the Tien Shan, the approach of dating deformed Late Quaternary geomorphic markers revealed that west of lake Issyk Kul (longitude ~75°E), at least eight thrust and reverse faults are currently active over two thirds of the entire width of the orogen, with individual fault

* Corresponding author. Fax: +49 251 83 33 933.
E-mail address: rahetzel@uni-muenster.de (R. Hetzel).

0033-5894/$ – see front matter © 2013 University of Washington. Published by Elsevier Inc. All rights reserved.
http://dx.doi.org/10.1016/j.yqres.2013.10.016

slip rates ranging from ~0.1 to ~3 mm/a (Thompson et al., 2002). Farther east in the Kungej Alatau north of Issyk Kul (Fig. 1b), slip rates for south-verging thrust faults and folds fall in the range between ~0.07 and ~0.37 mm/a (Bowman et al., 2004; Selander et al., 2012). In the Chinese Tien Shan two studies documented an eastward decrease in the shortening rate along the southern front of the mountain belt (Brown et al., 1998; Hubert-Ferrari et al., 2005). Near the town of Aksu at longitude 81°E, the minimum shortening rate is ~7 mm/a over the last ~13 ka (Hubert-Ferrari et al., 2005), whereas still farther east at longitude 85°E an upper limit of ~2 mm/a for the slip rate of the range-bounding reverse fault was provided on a similar time scale (Brown et al., 1998). Across the northern mountain front of the Boro Horo Shan (Fig. 1a), an early study that did not use numerical dating estimated a millennial shortening rate of 3.0 ± 1.5 mm/a based on the assumption that offset fluvial terraces are early Holocene in age (Avouac et al., 1993).

On longer time scales of 10^6 to 10^7 yr shortening rates at the southern and northern margins of the Tien Shan were inferred from the restoration of folds and geological cross sections (e.g. Yin et al., 1998; Burchfiel et al., 1999; Bullen et al., 2003; Scharer et al., 2004; Charreau et al., 2008), in combination with low-temperature thermochronology (Sobel et al., 2006; Jolivet et al., 2010). Comparing the deformation rates obtained on different time scales allows testing whether or not short-term rates inferred by geodetic methods are representative for a millennial or even a million-year time scale. Furthermore, the results of these different methods may enable us to resolve how the spatial distribution of deformation across the orogen has evolved through time.

In this study, we constrain the slip rate of the range-bounding thrust fault at the southern mountain front of the Dzungarian Alatau in southeast Kazakhstan (Fig. 1b) by terrace mapping, topographic profiling, and ^{10}Be surface exposure dating (e.g. Gosse and Phillips, 2001). The Dzungarian Alatau is probably the least studied region in the entire Tien Shan orogenic system and so far no quantitative data on Late Quaternary deformation rates are available for this 300-km-long mountain belt.

Study area

The study area is situated at the southern front of the Dzungarian Alatau, a mountain range that runs parallel to the E–W-trending Ili basin and the Tien Shan farther to the south (Fig. 1b). The Dzungarian Alatau has a complex basement comprising Proterozoic to Early Mesozoic metamorphic, sedimentary and igneous rocks (Bekzhanov, 1997). These rocks are interpreted as Proterozoic continental basement sutured in the north to Early Paleozoic to Carboniferous accretion complexes and overlain in the south by a Devonian to Permian active continental margin arc (Petrov et al., 2007; Windley et al., 2007). The modern mountain front in the south is defined by the 160-km-long, north-dipping Usek thrust fault that extends eastward to the region where the Usek River enters the Ili basin (Fig. 2). The Usek thrust fault has uplifted and emplaced Paleozoic basement rocks over Neogene and Quaternary sediments. Farther to the south, Devonian and Carboniferous basement rocks of the smaller Duyantau range are uplifted by steep thrust faults that dip to the northwest and southeast, respectively (Fig. 2) (Kober et al., 2013). The wide piedmont of the Duyantau range slopes gently toward the Ili basin and consists of different generations of Quaternary pediments and alluvial fans, which rest unconformably on folded Cenozoic sediments. These light-colored, fine-grained Cenozoic strata are dominated by fluvial sediments with interbedded lake deposits and are deformed by open folds with low amplitudes and east–west trending fold axes (Kober et al., 2013). The overlying Quaternary alluvial gravels are less than a few tens of meters thick and are slightly warped along an east-trending monocline near the floodplain of the Ili River (Fig. 2).

The Duyantau pop-up structure and the Lesnovka and Taldy anticlines plunge eastward and therefore no Paleozoic basement is exposed near the Usek River, which has formed a flight of well-preserved terraces that can be followed for ~15 km (Fig. 3). On the basis of field investigations and remote sensing we distinguish five major terrace levels, T_1–T_5, with the highest one (T_5) reaching an elevation of up to ~300 m above the Usek River. All terraces are sparsely vegetated by grass. Terrace T_1 is developed near the mountain front east of the Usek River. The other four terraces (T_2–T_5) are well preserved between the Taldy and Lesnovka anticlines (Fig. 3). The vertical distance between the different terrace levels T_2 to T_5 is between ~50 and ~70 m east of the Usek River (Fig. 4). At latitude 44°22.5′N, the terraces T_2–T_5 are at elevations of ~40 m (T_2), ~110 m (T_3), ~160 m (T_4), and ~230 m (T_5) above the bed of the Usek River.

At the mountain front farther north, terrace T_4 has been displaced by the Usek thrust fault (Fig. 3), which has formed a >100-m-high fault scarp. In the downthrown footwall block the well preserved terrace tread extends east–west for ~1.5 km, whereas in the uplifted hanging wall a considerable portion of the original terrace tread has been eroded. Still, two elongate parts of terrace T_4 are well preserved in the hanging wall (Figs. 3, 5a) and have a similar appearance in the field as the terrace tread in the footwall. A secondary, ~10-m-high scarp is present

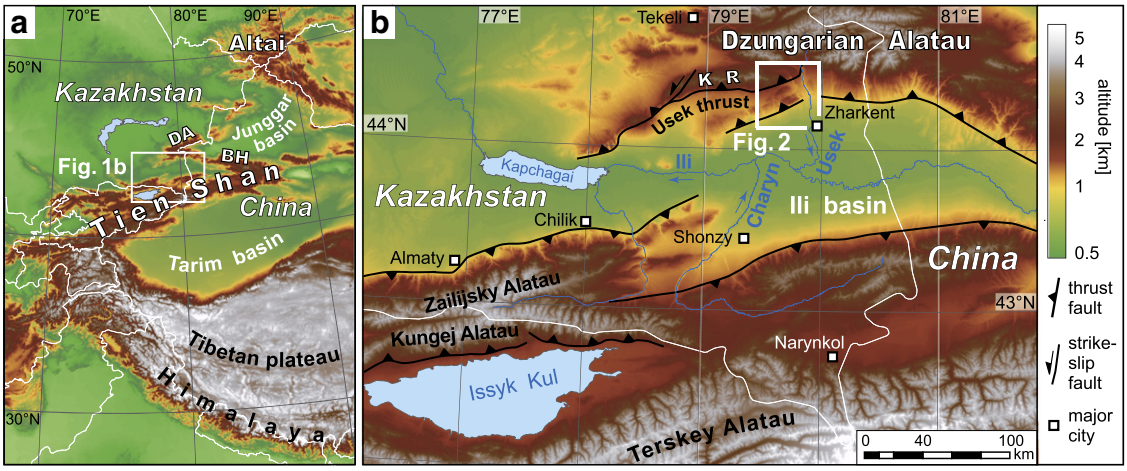

Figure 1. (a) Digital elevation model showing the location of the Tien Shan mountain belt, the Dzungarian Alatau (DA), and the Boro Horo Shan (BH). The white rectangle marks the location of b. (b) Digital elevation model with the location of the study area (white rectangle) at the southern mountain front of the Dzungarian Alatau. Also indicated is the Koyandytau Range (KR) traversed by a major left-lateral strike-slip fault.

https://doi.org/10.1016/j.yqres.2013.10.016 Published online by Cambridge University Press

in the footwall of the Usek thrust fault. We acquired two topographic profiles across the composite Usek fault scarp using differential GPS in order to quantify the total vertical offset on the underlying fault. The individual points of each profile were projected onto vertical planes oriented perpendicular to the fault strike. The two profiles constrain the total vertical displacement since the formation of terrace T_4 to ~132 ± 10 m (Fig. 6).

The fault plane of the Usek thrust fault is not well-exposed, but using the vertical and cross-strike horizontal distances measured between the point where the Usek thrust crosses our transect and another one where it reaches the Usek valley floor, a dip angle of ca. 45° can be estimated. For this estimate to be accurate, the fault must be planar. In fact, the trend of the thrust trace is not constant between the two observation points, but turns into a more northerly direction close to the Usek River (Figs. 2, 3). This geometry suggests that the two points are not located on a fault plane of constant strike and dip, but on a curved fault surface which is concave to the north. If this interpretation is correct, the dip of the Usek fault beneath the scarp is steeper than 45°, consistent with observations on other, exposed basement thrusts in the area which have dips of 50–70°. Following these considerations, we have used a dip range of 45–70° to calculate horizontal shortening rates.

^{10}Be surface exposure dating

Sampling strategy

For exposure dating we targeted terrace level T_4 at two sites along the Usek River (Fig. 3). We also sampled the proximal and distal parts of an alluvial fan in the southern piedmont of the Duyantau range (Fig. 2) to evaluate the age of depositional surfaces in an area not sourced by the Usek River. In the following, we describe our sampling strategy at these sites and explain how the potential presence of an inherited cosmogenic nuclide component can be corrected for. Inherited cosmogenic nuclides are generated prior to deposition during erosion of the host rock and sedimentary transport (e.g. Anderson et al., 1996). All samples for exposure dating were taken from the flattest and most pristine parts of the respective terrace and alluvial fan surfaces.

The first sampling site on terrace T_4 is located in the uplifted hanging wall of the Usek thrust fault (Fig. 3) and was sampled to determine the slip rate of this fault. The southern part of the flat terrace in the fault hanging wall has a size of about 400 × 600 m, is covered by grass, and appears to be well preserved (Fig. 5a). Small pits that we excavated on the terrace showed a clearly recognizable bedding in the terrace

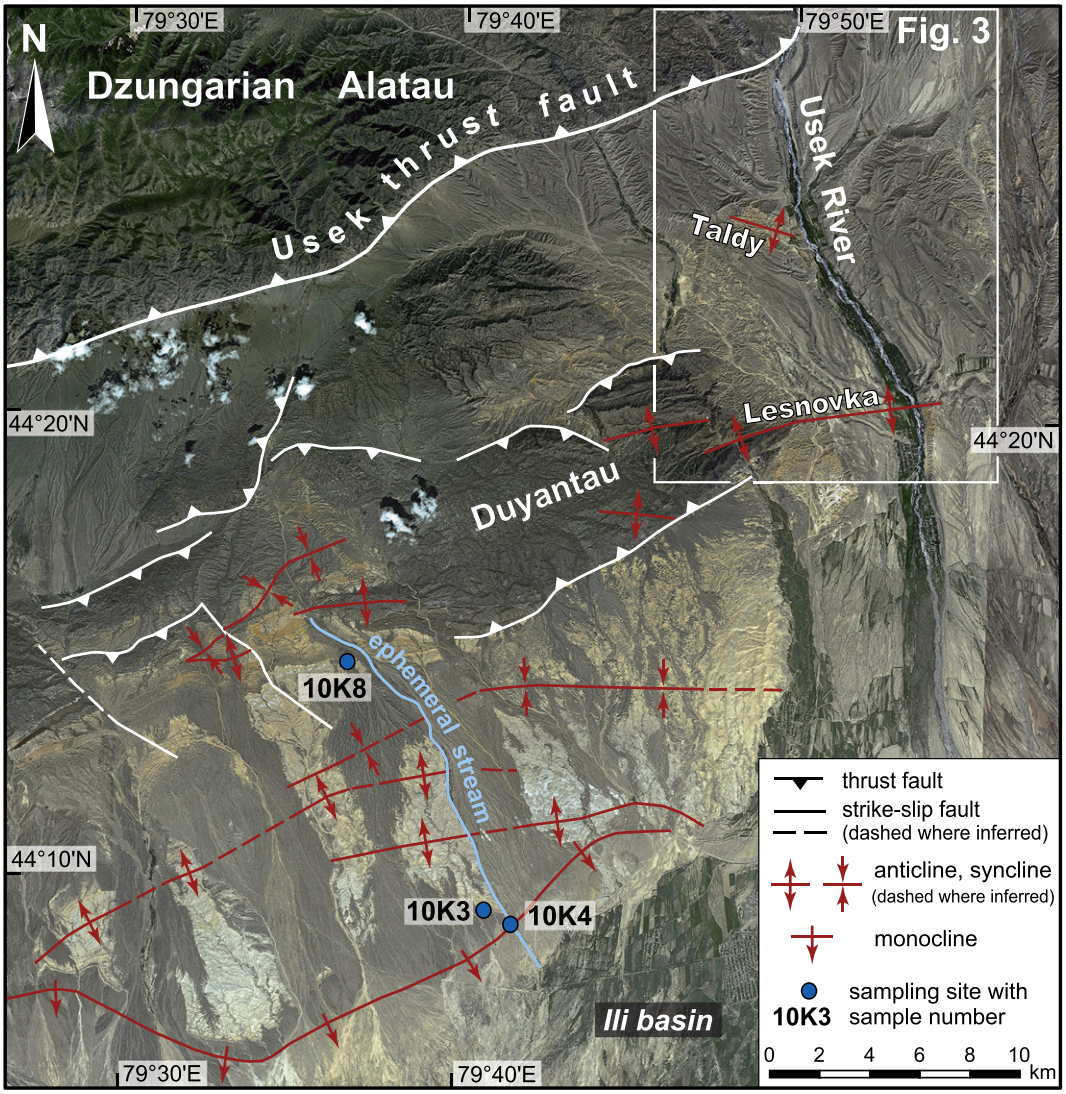

Figure 2. Tectonic map of the study area in the southern foreland of the Dzungarian Alatau, Kazakhstan, showing Quaternary active faults (white in map, black in legend). The white rectangle marks the area shown in Fig. 3. Ephemeral channels that have incised the coalesced alluvial fan south of the Duyantau range expose Neogene sediments, which appear in whitish color. For location of the map see Fig. 1b. The base image is a SPOT satellite image from Google Earth with a spatial resolution of 15 m (acquisition date: June 6, 2005).

https://doi.org/10.1016/j.yqres.2013.10.016 Published online by Cambridge University Press

deposits from a depth of 10–12 cm downwards. Clasts in the bedded terrace deposits have thin (<1 mm) carbonate rinds at their bottom. Boulders with a length of up to 90 cm occur on the terrace surface, presumably because of its proximity to the mountain front. The presence of desert varnish and lichen on the upper side of such boulders suggests that they have remained in a stable position for considerable time. We took three samples from the flat, upper side of two granite boulders (samples 10K9 and 10K11) and one quartzite boulder (sample 10K10) (Figs. 5b–d). The planar tops of these boulders stood 4–9 cm above the surrounding surface, while their main parts were embedded in the terrace deposits. Although several previous studies have shown that the inherited nuclide component of large boulders is often negligible (e.g. Zehfuss et al., 2001; Palumbo et al., 2009), a recent study documented highly variable exposure ages for boulders on terraces at the eastern front of the Andes, thus revealing that the inheritance of boulders is not necessarily negligible (Schmidt et al., 2011). We therefore

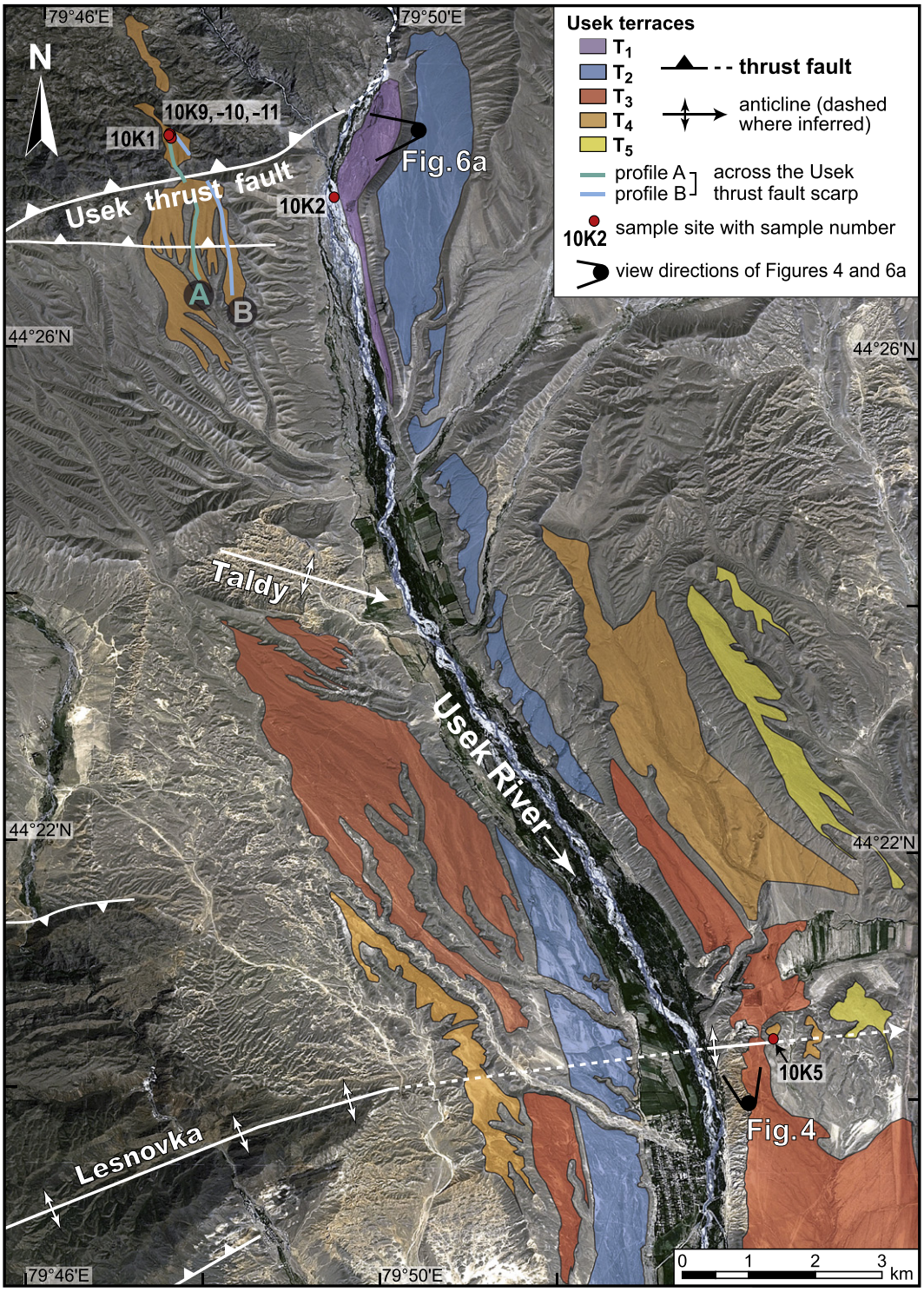

Figure 3. Map showing the extent of the terraces T_1–T_5 along Usek River and the range-bounding Usek thrust fault at the front of the Dzungarian Alatau. The positions of two fault scarp profiles shown in Fig. 6c are indicated as thick lines labeled A and B. For location of the map see Fig. 2. The base image is a SPOT satellite image from Google Earth with a spatial resolution of 15 m (acquisition date: June 6, 2005).

https://doi.org/10.1016/j.yqres.2013.10.016 Published online by Cambridge University Press

also applied an alternative dating approach, which assumes that the inherited nuclide component of a terrace sample consisting of amalgamated pebbles can be determined by analyzing a similar sample from the active river bed. Sample 10K1 consists of 62 quartz pebbles with a size of 1–6 cm and was collected on terrace T_4 from an area with a size of about 100 × 100 m. To evaluate the inherited nuclide concentration of this sample, we took a sample composed of 48 quartz pebbles with a size of 2–6 cm from the modern Usek River (10K2; for location see Fig. 3).

The second sampling site on terrace T_4 is situated 15 km farther south and east of the Usek River. Here, an isolated patch of T_4 with a diameter of ~200 m is almost entirely surrounded by the lower terrace T_3 and thus shielded from the deposition of material derived from the higher terrace T_5 (Fig. 3). The planar terrace lacks even minor erosional rills and is well preserved (Fig. 5e). In the interior part, the terrace is partially covered by a ≤33-cm-thick loess layer that thins and gradually disappears toward the terrace edges. A 10–20 m wide area along the southern edge of the terrace exhibits angular to subangular clasts with a size of 0.5–5 cm at the surface that are coated with desert varnish. As exposed boulders are rare owing to the thin loess cover on the terrace, we excavated a 1.8-m-deep pit near the southern terrace margin (Fig. 5e) and took four sand samples along a depth profile: a surface sample (10K5) and three subsurface samples (10K5A, -B, -C). Such depth profiles allow us to quantify both inherited and post-depositional nuclide components (e.g. Hancock et al., 1999; Siame et al., 2004; Schmidt et al., 2011). We sieved the sand samples in the field to obtain the 0.25–2.0 mm size fraction. The walls of the pit exposed bedded terrace deposits from a depth of 34 cm downward; below this depth all clasts and boulders have a thin (~0.1 mm) rind of pedogenic carbonate at their bottom side.

The sampling area in the southern piedmont of the Duyantau range is located ~20 km west of the Usek River (Fig. 2). Here, a gently southward-dipping, inactive alluvial fan with a width of ~10 km is slightly warped along a monocline, which marks the transition to the Ili basin. The flat surface of the coalesced alluvial fan shows a moderately to well developed desert pavement with subangular clasts 1–10 cm in size on the surface. The surface is sparsely vegetated by grass in the north but farther south the vegetation disappears almost completely (Fig. S1). The alluvial fan surface is inactive today. Younger ephemeral channels have incised below the alluvial fan gravels and exposed Neogene sediments (Fig. 2). To date the proximal and distal parts of the alluvial fan, respectively, we took two samples (10K8 and 10K3) (Fig. S1). The northern sample (10K8) is composed of 250 quartz pebbles, which were taken from an area 150 × 50 m in size. The sample from the southern part (10K3) consists of 196 quartz pebbles collected from an area with a diameter of about 30 m. In order to correct for an inherited nuclide component in the two samples, we amalgamated 99 quartz pebbles (10K4) in the bed of the active ephemeral channel whose upstream part sourced the sampled alluvial fan in the past (Fig. 2). The size of the pebbles in all three samples varied between 0.5 and 5 cm.

Sample preparation and ^{10}Be analysis

The quartz pebbles of the amalgamated samples 10K1 and -2 had a size range of 1–6 cm and 2–6 cm, respectively. To ensure that each pebble contributed a roughly equal amount of mass to the samples, we used only a part of those pebbles ≥3 cm. For the three samples 10K3, -4, and -8, which had a size range of 0.5–5 cm, this size limit was set to 2 cm. After crushing the quartz pebbles and the rock material from the boulders, all samples were sieved and the 250–500 μm size fraction was washed and the magnetic grains were removed. The samples were treated following procedures introduced by Kohl and Nishiizumi (1992) to obtain clean quartz. Firstly, the samples were leached in 20% HCl at ~80°C to dissolve carbonates and iron oxides. Secondly, they were etched three to four times in 1% HF/1% HNO_3 in a heated ultrasonic bath at 80°C to remove meteoric ^{10}Be. Subsequently, most samples were further purified by alternating etching steps in aqua regia and ~13% HF at ~120°C (Goethals et al., 2009). The purity of the quartz separates was checked with ICP-OES. After addition of ~0.3 mg of Be carrier, the quartz samples (30–40 g) were dissolved, Be was separated by successive anion and cation exchange columns and precipitated at pH 8–9 as $Be(OH)_2$. Following the transformation to BeO at 1000°C and target preparation, ^{10}Be was analyzed at the accelerator mass spectrometer (AMS) facility of ETH Zurich (Kubik and Christl, 2010). The blank-corrected ^{10}Be concentrations reported in Table 1 are normalized to the secondary ETH standard S2007N, which has a nominal $^{10}Be/^{9}Be$ ratio of 28.1×10^{-12} (Kubik and Christl, 2010) considering the ^{10}Be half-life of 1.387 Ma (Chmeleff et al., 2010; Korschinek et al., 2010). This secondary standard is calibrated to the primary standard ICN 01-5-1 (Nishiizumi et al., 2007; Kubik and Christl, 2010).

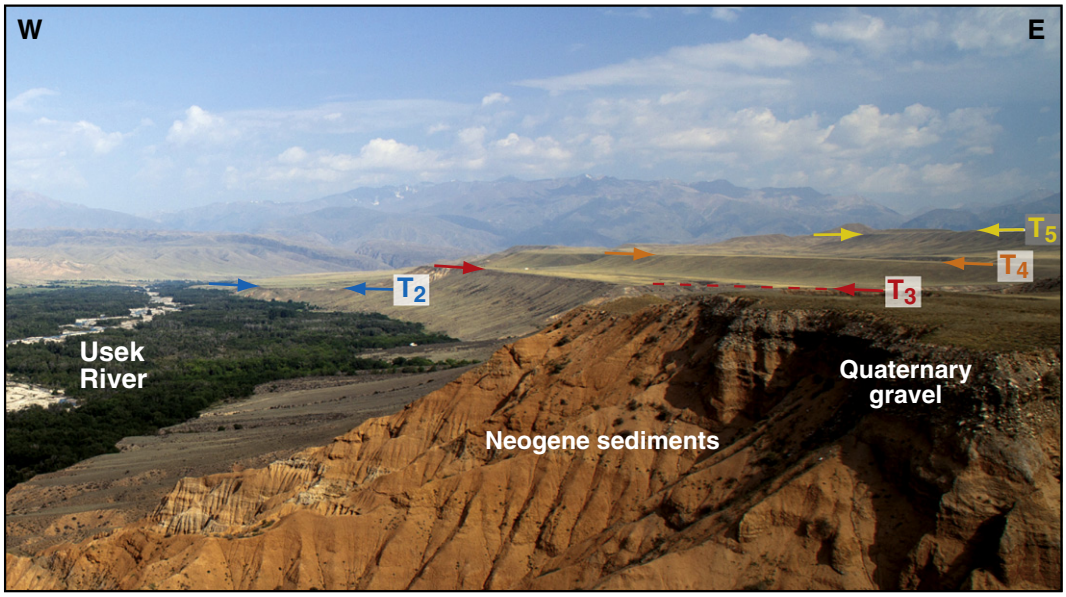

Figure 4. Northward view on terrace levels T_2–T_5 east of Usek River with their rather uniform vertical spacing. In the foreground Neogene sediments are covered by coarse Quaternary gravels above the strath of terrace T_3. The Dzungarian Alatau can be seen in the background. The view point from which the picture was taken is indicated in Fig. 3.

https://doi.org/10.1016/j.yqres.2013.10.016 Published online by Cambridge University Press

Calculation of ^{10}Be exposure ages and results

We calculated two sets of ^{10}Be exposure ages (Table 1) with the CRONUS-Earth online calculator (Balco et al., 2008; http://hess.ess.washington.edu) using the time-independent scaling model of Lal (1991)/Stone (2000). Before the age calculation, the ^{10}Be concentrations of the three amalgamated quartz pebbles (10K1, -K3, -K8) were corrected for an inherited nuclide component based on the ^{10}Be concentrations of the Usek River sample (10K2) and the sample from the ephemeral channel (10K4), respectively. The measured ^{10}Be concentrations of the two latter samples were rounded to the nearest value and conservative errors of ± 50% and ± 30%, respectively, were adopted because the cosmogenic nuclide concentration of pebbles from active rivers or ephemeral streams may deviate from the one in pebbles of the associated depositional surfaces (Hetzel et al., 2004; Blisniuk et al., 2012). This approach yielded values of $7.0 \pm 3.5 \times 10^4$ at/g (based on the ^{10}Be concentration of $7.47 \pm 0.37 \times 10^4$ at/g in 10K2) and $17.0 \pm 5.1 \times 10^4$ at/g (based on the ^{10}Be concentration of $16.7 \pm 1.0 \times 10^4$ at/g in 10K4), respectively, which were used to correct for the inheritance. A potential shielding by snow was not taken into account owing to the arid climate in the study region, with precipitation falling largely as rain in the summer months (Cheng et al., 2012). The following example calculation shows that this approach is reasonable. The presence of a 40-cm-thick snow cover with a density of 0.25 g/cm^3 (i.e. 100 mm water equivalent) for four months per year would change the ^{10}Be concentrations, and hence the ages, by only 2%.

The first set of ^{10}Be ages was determined with the assumption of zero erosion (Table 1). Provided that inheritance was adequately

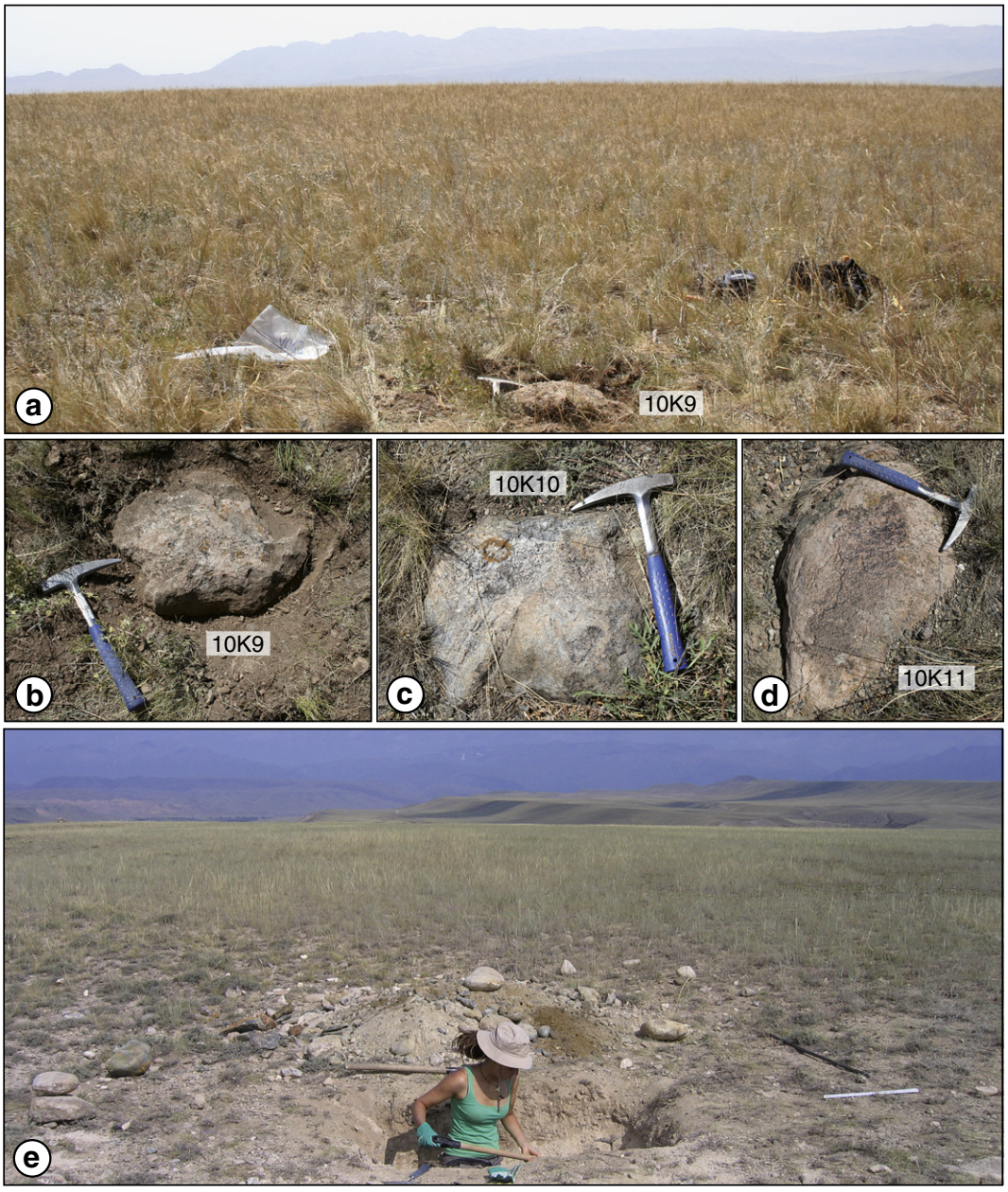

Figure 5. Photographs of the two sampling sites on terrace T_4 along the Usek River and close-up pictures of the three boulders sampled in the hanging wall of the Usek thrust fault. For location of the sampling sites see Fig. 3. (a) Overview of the flat, grass-covered terrace surface T_4 in the hanging wall of the Usek thrust fault. (b) Granite boulder with a diameter of 45 cm. We took sample 10K9 from the top of the boulder, which stands 4 cm above the surrounding ground. (c) The quartzite boulder from which we took sample 10K10 has a diameter of 42 cm and stands 7 cm above the terrace. (d) Elongate granite boulder with a length of 88 cm and dark desert varnish on the upper side. Sample 10K11 was taken from the top of this boulder, which stands 9 cm above the terrace. (e) Overview of the well preserved, sparsely vegetated terrace T_4 east of Usek River where we took four samples (10K5, 10K5A, -B, -C) along a depth profile from the pit seen in the foreground. View is toward the north.

https://doi.org/10.1016/j.yqres.2013.10.016 Published online by Cambridge University Press

corrected for (i.e. in the amalgamated pebbles) or is negligible (in the boulders), these ages represent *minimum* ages because either erosion or the presence of a temporal cover (e.g. snow) would have lowered the ^{10}Be production rate at the present-day surface. Given the high ages of roughly 300 ka obtained for the boulders and the quartz pebbles from terrace T_4, it is almost certain that a limited amount of material was removed from the surface by erosion. Hence, the ages calculated with the zero-erosion assumption underestimate the true age of the respective surfaces. In order to take erosion into account, we calculated a second set of ages using an erosion rate of 0.5 mm/ka (Table 1; the choice of the erosion rate and the related amount of erosion are discussed in the next section). This approach yielded ^{10}Be ages of 378 ± 14 ka, 301 ± 11 ka, and 363 ± 14 ka (internal 1σ error) for the three boulders from the hanging wall of the Usek thrust fault (samples 10K9, -10, -11), which were calculated by assuming a negligible inheritance. The fact that the independent ^{10}Be age of 357 ± 14 ka for the quartz pebbles agrees with the two oldest boulder ages (Table 1) provides strong evidence that this assumption is justified.

The depth profile consisting of four sand samples from terrace T_4 east of the Usek River was evaluated with the method of Hidy et al. (2010), which uses Monte Carlo simulations to determine the most plausible values for the inherited component and the post-depositional ^{10}Be concentration at the surface. As the ^{10}Be concentration of the surface sample is much lower than expected from the ^{10}Be concentrations of the subsurface samples (Fig. 7), it was excluded from the numerical simulation. For the simulation we chose the following values: (1) a spallogenic ^{10}Be surface production rate of 11.15 at/g/a determined with the CRONUS-Earth calculator, (2) an effective neutron attenuation length of 160 ± 8 g cm^2 (Gosse and Phillips, 2001), (3) a bulk density varying between 2.1 and 2.3 g/cm^3, (4) an age range between 250 ka and 450 ka, (5) a conservative range for the inheritance of 7–40 × 10^4 at/g, and (6) a ^{10}Be half-life of 1.387 ± 0.012 Ma (Chmeleff et al., 2010; Korschinek et al., 2010). The ^{10}Be production by slow and fast muons according to the experimental results of Heisinger et al. (2002a, 2002b) is implemented in the method of Hidy et al. (2010). In the modeling procedure the erosion rate could not be treated as a free parameter, because the number of samples (n = 3) must be greater than the number of free parameters to be determined (which are inheritance and age) to obtain statistically robust results (Hidy et al., 2010). The best-fit profile from 100,000 solutions resulted in an inheritance of 19 $^{+14}/_{-11}$ × 10^4 at/g, which was subtracted from the modeled surface concentration of 353 $^{+48}/_{-17}$ × 10^4 at/g to yield a post-depositional ^{10}Be concentration of 335 $^{+50}/_{-21}$ × 10^4 at/g. The latter was used as input for the CRONUS-Earth calculator to determine an exposure age of 360 $^{+67}/_{-28}$ ka for terrace T_4, again using an erosion rate of 0.5 mm/ka (Table 1).

The two pebble samples collected from the alluvial fan in the piedmont of the Duyantau range (10K3, 10K8) yielded inheritance-corrected ^{10}Be ages of 127.3 ± 7.4 ka and 83.4 ± 8.4 ka. Finally, we note that the use of the other scaling schemes implemented in the CRONUS-Earth online calculator (Dunai, 2001; Lifton et al., 2005; Desilets et al., 2006) would result in exposure ages that deviate by less than 8% from those reported in Table 1.

Discussion

Timing of terrace formation

From the four samples taken on terrace T_4 in the hanging wall of the Usek thrust, three have ^{10}Be ages that agree within internal uncertainty. Two boulders (10K9 and -11) yielded ages of 378 ± 14 ka and 363 ± 14 ka, respectively, while the amalgamated quartz pebbles (10K1) gave an age of 357 ± 14 ka (Table 1). The latter has been

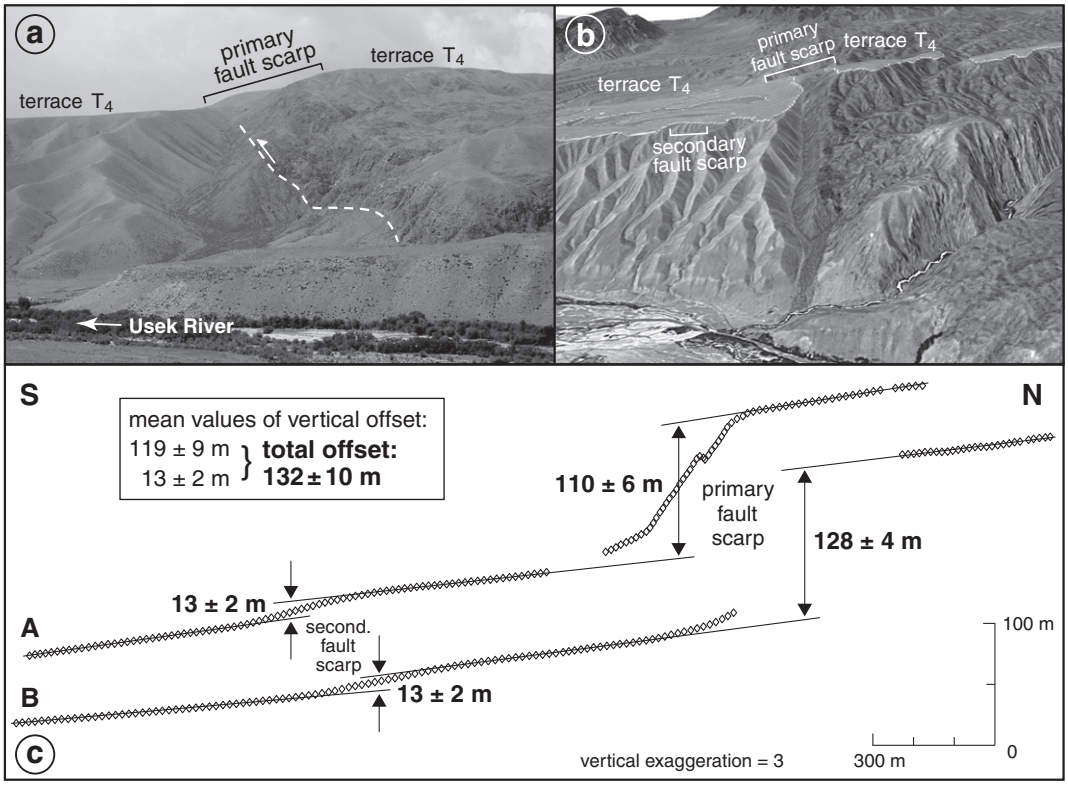

Figure 6. Thrust fault scarp at the mountain front of the Dzungarian Alatau west of Usek River. (a) Photograph of the fault scarp, which offsets the river terrace T_4. In the foreground the approximate trace of the main/primary thrust fault (>100 m offset) separating basement rocks in the hanging wall from Neogene sediments in the footwall is indicated by the white dashed line. View direction is to the west. The fault scarp related to the secondary fault is located to the left of the image. The view point from which the picture was taken is indicated in Fig. 3. (b) Perspective-view image (generated with Google Earth) of the primary fault scarp in which the offset terrace T_4 is outlined by the thin white line. Vertical exaggeration is 2. View direction is to the west. (c) Two topographic profiles across the composite thrust fault scarp with vertical displacement values. The total vertical offset is 132 ± 10 m. The location of the two pictures and the scarp profiles is shown in Fig. 3.

https://doi.org/10.1016/j.yqres.2013.10.016 Published online by Cambridge University Press

Table 1
^{10}Be concentrations, production rates and exposure ages from terraces at the southern front of the Dzungarian Alatau, Kazakhstan.

Sample type and number	Geomorphic position	Latitude	Longitude	Elevation	Sample thickness	Topogr. shielding	^{10}Be conc.[a] 1σ error	^{10}Be conc.[b] 1σ error	Product. rate (spallation)	Production rate (muons)	^{10}Be age (ε = 0)[c] int. (ext.) 1σ error	^{10}Be age (ε = 0.5 mm/ka)[c] int. (ext.) 1σ error
		WGS 84										
		(°N)	(°E)	(m)	(cm)		(10^4 at/g)	(10^4 at/g)	(at/g/a)	(at/g/a)	(ka)	(ka)
Usek river terraces												
Terrace T_4: hanging wall of Usek thrust west of Usek river												
Boulders												
10K9	T_4	44.4622	79.7909	1757	6	0.9998	520 ± 15	–	17.20	0.316	321 ± 10 (32)	**378 ± 14 (45)**
10K10	T_4	44.4618	79.7909	1756	5	0.9998	437 ± 13	–	17.33	0.317	264.6 ± 8.5 (26)	**301 ± 11 (34)**
10K11	T_4	44.4624	79.7907	1757	6	0.9998	504 ± 15	–	17.20	0.316	311 ± 10 (31)	**363 ± 14 (43)**
Amalgamated quartz pebbles												
10K1	T_4	44.4623	79.7908	1757	3	0.9998	518 ± 16	511 ± 16	17.64	0.318	307 ± 10 (31)	**357 ± 14 (42)**
10K2	Usek river	44.4544	79.8255	1259	3	–	7.47 ± 0.37	–	–	–	–	–
Terrace T_4: east of Usek river												
Sand samples from depth profile												
10K5	T_4 (0–5 cm)	44.3412	79.9069	1132	5	0.9999	188.3 ± 5.7	–	10.78	0.259	178.3 ± 5.6 (17)	–
10K5A	T_4 (60–62 cm)	"	"	"	–	–	171.0 ± 6.7	–	–	–	–	–
10K5B	T_4 (116–119 cm)	"	"	"	–	–	92.6 ± 2.8	–	–	–	–	–
10K5C	T_4 (170–177 cm)	"	"	"	–	–	54.8 ± 2.6	–	–	–	–	–
10K5[d]	T_4	"	"	"	–	0.9999	–	335 (+50/−21)[d]	11.15	0.262	317 +51/−21 (+59/−37)	**360 +67/−28 (+77/−48)**
Alluvial fan at piedmont of Duyantau range												
Amalgamated quartz pebbles												
10K3	Southern fan	44.1556	79.6821	716	3	1.0000	79.7 ± 3.1	62.7 ± 6.0	7.71	0.226	80.6 ± 7.8 (11)	**83.4 ± 8.4 (11)**
10K8	Northern fan	44.2450	79.6115	1179	3	0.9999	152.1 ± 5.0	135.1 ± 7.2	11.27	0.264	120.7 ± 6.6 (13)	**127.3 ± 7.4 (14)**
10K4	Active channel	44.1502	79.6953	670	3	–	16.7 ± 1.0	–	–	–	–	–

[a] Blank-corrected ^{10}Be concentrations. Based on two process blanks a value of 0.137 ± 0.022 × 10^4 at/g was used for the blank correction. Propagated analytical errors (1σ) include the error of the counting statistics and the error of the blank correction. ^{10}Be concentrations were measured at ETH Zurich and are normalized to the secondary standard S2007N with a nominal ^{10}Be/^{9}Be ratio of 28.1 × 10^{-12} (Kubik and Christl, 2010).

[b] ^{10}Be concentrations of all samples – except the boulders – are corrected for an inherited nuclide component. To correct for the inheritance of sample 10K1 we used a value of 7.0 ± 3.5 × 10^4 at/g (based on sample 10K2 from Usek river). For samples 10K3 and 10K8 a value of 17.0 ± 5.1 × 10^4 at/g was used (based on sample 10K4 from an active ephemeral channel). The inheritance for the depth profile was derived from the three subsurface samples using the numerical modeling approach of Hidy et al. (2010) (for details see text).

[c] Exposure ages were calculated with the CRONUS-Earth ^{10}Be–^{26}Al calculator, version 2.2 with version 2.2.1 of the constant file (Balco et al., 2008; http://hess.ess.washington.edu), assuming a rock density of 2.7 g/cm^3 (except for the depth profile) and using the time-invariant production rate scaling model of Lal (1991)/Stone (2000). We report exposure ages for the assumption of zero erosion (ε = 0) and for an erosion rate of ε of 0.5 mm/ka. Internal uncertainties (int.) include errors from the counting statistics and the blank correction, whereas external (ext.) uncertainties also include the error of the production rate introduced by the scaling model.

[d] The reported post-depositional ^{10}Be concentration at the surface was derived from the three subsurface samples by applying the numerical approach of Hidy et al. (2010) (for details see text).

corrected for a small inherited nuclide component equivalent to 4 ± 2 ka. The close agreement between the three ages obtained by two different dating approaches (boulders versus amalgamated pebbles) indicates a negligible inheritance for the boulders and a common exposure history for all three samples. It is important to note that the calculated exposure ages depend on the erosion rate, for which we assumed a value of 0.5 mm/ka. This erosion rate combined with the ^{10}Be ages of ~360–380 ka implies that ~20 cm of material was removed from the terrace. Given the flatness of the sampled portions of terrace T_4 and the absence of erosional rills such a small amount of surface lowering seems not unreasonable (Figs. 5a, e). If the terraces were eroded at a higher rate, the exposure ages and the absolute amount of erosion would also be higher. For instance, an erosion rate of 1 mm/ka would increase the ^{10}Be ages to ~450–470 ka and the total amount of erosion to ~45 cm. We argue that such a relatively large amount of erosion is not supported by the microtopography of the terrace surfaces (Figs. 5a, e), although there is no method available to independently constrain the local erosion rate of a terrace surface exactly. A similarly low erosion rate of 0.5 mm/ka (as used in this study) was determined for a terrace with a ^{10}Be age of ~260 ka in Patagonia (Hein et al., 2009). Selander et al. (2012) used the similarity between a ^{10}Be exposure age of 85.6 ± 7.6 ka and an OSL age of 96.0 ± 8.6 (Bowman et al., 2004) for the same terrace near Issyk Kul to argue for a minimal amount of erosion (which they accordingly neglected when calculating ^{10}Be ages of ~80 to ~140 ka for three terraces). Finally, we note that the *maximum* erosion rate that can be derived from the ^{10}Be concentrations of the samples from terrace T_4 is ~2.1 mm/ka. This approach assumes, however, that the ^{10}Be concentrations have reached a steady-state between ^{10}Be production and removal of ^{10}Be by erosion and radioactive decay, a scenario which we consider unlikely.

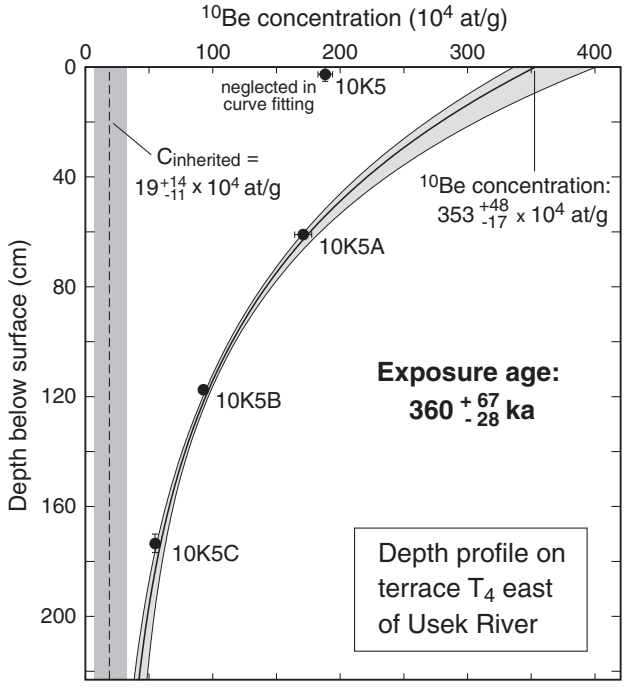

Figure 7. ^{10}Be depth profile on terrace T_4 east of Usek River, which consists of four sand samples (10K5, 10K5A, -B, and -C). The ^{10}Be concentrations of the samples (see Table 1) are shown as black circles with 1σ errors (error bars for the two lower samples are smaller than the data points). Vertical error bars reflect the width of the sampled depth interval (error bars for 10K5A and -B are smaller than the data points). The solid black line represents the best-fit regression through the ^{10}Be concentrations of the three subsurface samples obtained with the numerical model of Hidy et al. (2010). The gray shading shows the 1σ solution space of the model simulations. The dashed vertical line and the gray field indicate the inherited ^{10}Be component and its 1σ error. The post-depositional ^{10}Be concentration yields a ^{10}Be exposure age of 360 $^{+67}/_{-28}$ ka for an erosion rate of 0.5 mm/ka (Table 1). See text for details on the parameter space explored. The location of the sampling site is indicated in Fig. 3.

If the amount of ~20 cm erosion on terrace T_4 is roughly correct, it implies that the three boulders (which stand 4–9 cm above the terrace) were initially buried in the terrace deposits and were slowly exhumed. Neglecting the youngest boulder, we calculate an error-weighted mean age of 366 ± 8 ka from the ^{10}Be ages of the two oldest boulders and the age of the amalgamated pebbles using the internal errors (Table 1). Considering the systematic error of the sea level-high latitude ^{10}Be production rate and the error of the employed scaling model (cf. Balco et al., 2008), leads to a mean ^{10}Be age of 366 ± 37 ka (external uncertainty). This age constraint does not include the uncertainty associated with the simplifying assumption of a steady erosion rate of 0.5 mm/ka over the entire lifetime of the terrace. By increasing the error of the mean ^{10}Be age to ±60 ka, we account for possible erosion rates in the range between 0.3 and 0.7 mm/ka. When calculating the slip rate of the Usek thrust in the following section we thus use an age value of 366 ± 60 ka.

The three sand samples (10K5A, -B, -C) from the depth profile on terrace T_4 east of Usek River yielded a ^{10}Be age 360 $^{+67}/_{-28}$ ka (Table. 1). Note that for the depth profile simulation the surface sample (10K5) was neglected, because its ^{10}Be concentration is too low relative to the subsurface samples and incompatible with an exponential decrease of the nuclide concentration with depth. The agreement between the age constraints determined for terrace level T_4 at two widely separated locations lends support for the robustness of the exposure dating results. A ^{10}Be surface concentration that is inconsistent (i.e. too low) with the ^{10}Be concentrations measured in the subsurface samples from a depth profile was also reported in other studies (e.g. Perg et al., 2001; Matmon et al., 2006; Schmidt et al., 2011). There are several possible reasons why the surface sample from the depth profile has a low nuclide concentration and an apparent age that is too young (i.e. ~178 ka; Table 1). A mixing of near-surface sediment by bioturbation may have homogenized the ^{10}Be concentration in the mixed layer, thereby reducing the ^{10}Be concentration at the surface (cf. Granger and Riebe, 2007). However, in the excavated pit the terrace deposits are bedded below a depth of 34 cm and only the sediment at shallower depth could have been mixed. Mixing of a 34-cm-thick layer would reduce the ^{10}Be surface concentration by ~20%, which is insufficient to explain the low concentration observed in the surface sample. Another process that may explain the low ^{10}Be concentration of the surface sample is the inflation of sand with a low ^{10}Be concentration. This material cannot be derived from the same terrace, but may have originated from the active floodplain of the Usek River or from active alluvial fans at the mountain front.

The two samples from the alluvial fan surface south of the Duyantau range (Fig. 2) yielded exposure ages of 127.3 ± 7.4 ka and 83.4 ± 8.4 ka (Table 1). These ages are interpreted to indicate that the alluvial fan surface becomes younger toward the south (i.e. with increasing distance from the mountain front). This southward younging likely reflects the progressive incision of the ephemeral stream located east of the two sample sites into the alluvial fan deposits (Fig. 2). Hence, the abandonment of the alluvial fan was a diachronous process that propagated toward the foreland and started earlier in the north than in the south. The fact that the alluvial surface is slightly warped along the NE-trending monocline, which marks the transition to the Ili basin, indicates ongoing deformation and uplift in the southern part of the alluvial fan (Fig. 2).

Slip rate of the Usek fault and comparison with geodetic and geologic shortening estimates

The T_4 surface is vertically offset 132 ± 10 m across the Usek thrust fault, which we determined by measuring two topographic profiles across the terrace (Fig. 6c). Combined with the ^{10}Be age constraint of 366 ± 60 ka for the offset terrace T_4 this offset yields a vertical fault slip rate of 0.36 ± 0.07 mm/a (1σ error) for the Usek thrust fault. When calculating this rate, we assumed that the uncertainties in age

https://doi.org/10.1016/j.yqres.2013.10.016 Published online by Cambridge University Press

and vertical displacement have a Gaussian distribution (cf. Zechar and Frankel, 2009). Considering the fault dip of 45–70° estimated for the Usek thrust fault as explained above, we obtain a horizontal shortening rate of 0.25 (+0.09/−0.08) mm/a (1σ error). This rate was determined by assuming a Boxcar uncertainty model for the horizontal displacement with minimum and maximum values of 48 m and 132 m, respectively, and a Gaussian distribution for the age uncertainty (cf. Zechar and Frankel, 2009).

The slip rate of the Usek fault is similar to slip rate values of ~0.07 mm/a to ~0.38 mm/a determined for south-directed thrust faults at the southern front of the Kungej Alatau (Fig. 1b) by Selander et al. (2012). These authors also estimated slip rates of 0.8 ± 0.5 mm/a and 0.4 ± 0.3 mm/a for two north-directed thrust faults in the northeastern Zailijsky Alatau southeast of Chilik (see Fig. 1b for location) by simply assuming that the displaced terraces have an age of 100 ± 30 ka. In the Tien Shan west of Issyk Kul, slip rates obtained for thrust faults are more variable, with values ranging from ~0.1 to ~3 mm/a (Thompson et al., 2002). Overall, these results show that many of the range-bounding thrust faults in the Dzungarian Alatau and the Tien Shan move at rather low rates of <1 mm/a.

Values for the shortening rate on a geological time scale of millions of years are not available for the Dzungarian Alatau. Farther east, at the mountain front of the Boro Horo Shan, shortening rates derived from syntectonic growth strata of individual fault-controlled anticlines are ~1 mm/a over the last few million years (e.g. Charreau et al., 2008). The cumulative shortening rate across the two to three rows of anticlines present between ~83° and ~87°E is about 3–6 mm/a (Burchfiel et al., 1999; Daëron et al., 2007; Charreau et al., 2008; Li et al., 2011). Although this value is still not well-constrained it appears to be roughly similar to the GPS-based shortening rate (Yang et al., 2008; Li et al., 2011).

The current shortening rate across the entire Tien Shan decreases from ~20 mm/a in the west to ~9 mm in the east (Zubovich et al., 2010). If we take GPS-derived shortening rates as indicative of shortening rates on the time scale of our measured ages, it appears that the orogenic deformation must be partitioned on several active thrust faults running subparallel to the strike of the Tien Shan. A small fraction of the crustal shortening may also be accommodated on left-lateral strike-slip faults trending WSW–ENE, which were documented northwest of Issyk Kul by Selander et al. (2012).

To compare our shortening rate for the Usek thrust fault in more detail with the GPS-based deformation pattern across the Dzungarian Alatau, we used the data of Zubovich et al. (2010), who plotted GPS velocity vectors on a series of ~N–S profiles. Their profile at longitude ~80°E indicates a north–south contraction of 1–3 mm/a across the Dzungarian Alatau (Zubovich et al., 2010; their fig. 4d). This geodetically determined shortening rate has a considerable uncertainty because the errors in the north-directed velocity components of the individual stations reach up to ±0.8 mm/a. If the shortening rate is in the lower end of the range of 1–3 mm/a, the active structures at the southern mountain front of the Dzungarian Alatau (Fig. 2) may account for most, if not all, of the current shortening. These structures include the Usek thrust fault (Fig. 3) with a shortening rate of 0.25 (+0.09/−0.08) mm/a, the two thrust faults bounding the Duyantau pop-up structure, and the monocline defining the boundary between the piedmont of the Duyantau range and the Ili basin farther south (Fig. 2). Whether active thrust faults or folds are present at the northern margin of the Dzungarian Alatau remains to be investigated.

Conclusions

Surface exposure dating of river terraces and alluvial fans with the cosmogenic nuclide ^{10}Be provides insight into the ongoing crustal shortening in the Dzungarian Alatau. Active deformation at the southern front of the Dzungarian Alatau occurs on the 160-km-long range-bounding Usek thrust fault – which has a vertical slip rate of 0.36 ± 0.07 mm/a over the past ~400 ka – and on minor thrust faults and monoclines in the southern piedmont of the Dzungarian Alatau. Our investigations and previous studies in the Tien Shan farther south demonstrate the importance of studying fault scarps and quantifying slip rates of individual faults, because the active deformation on slowly slipping structures cannot be resolved by GPS measurements given the coarse station spacing. Quantifying slip rates of faults on millennial time scale by dating deformed landforms such as river terraces is also essential for evaluating the pattern of distributed deformation across the Tien Shan orogenic system. Both morphotectonic studies and GPS data support the notion that the ongoing deformation is partitioned on several active structures across the entire Tien Shan orogenic system.

Supplementary data to this article can be found online at http://dx.doi.org/10.1016/j.yqres.2013.10.016.

Acknowledgments

We are most grateful to Aleksandr Esmintsev (Academy of Sciences, Almaty) for drawing our attention to the Usek River area and guiding us on our first field trip. We thank Anne Niehus for help with the sample preparation, Veronica Rapelius for ICP-OES analysis of the leached quartz separates, Marcus Strobl for help with the MATLAB files of Zechar and Frankel (2009), and Peter Kubik for AMS analysis. A detailed and thorough review by Ryan Gold greatly improved the focus and clarity of the paper. Funding of this project by the German Research Foundation (DFG; grant no. KL 495/15-1) is gratefully acknowledged.

References

Abdrakhmatov, K.Y., et al., 1996. Relatively recent construction of the Tien Shan inferred from GPS measurements of present-day crustal deformation rates. Nature 384, 450–453.

Anderson, R.S., Repka, J.L., Dick, G.S., 1996. Explicit treatment of inheritance in dating depositional surfaces using in situ ^{10}Be and ^{26}Al. Geology 24, 47–51.

Avouac, J.P., Tapponnier, P., Bai, M., You, H., Wang, G., 1993. Active thrusting and folding along the northern Tien Shan and Late Cenozoic rotation of the Tarim plate relative to Dzungaria and Kazakhstan. Journal of Geophysical Research 98, 6755–6804.

Balco, G., Stone, J.O., Lifton, N.A., Dunai, T.J., 2008. A complete and easily accessible means of calculating surface exposure ages or erosion rates from ^{10}Be and ^{26}Al measurements. Quaternary Geochronology 3, 174–195.

Bekzhanov G.R. (Chief editor), Geological map of Kazakhstan. Scale 1:1.000.000, ВСЕГЕИ (VSEGEI, All-Russian Research Institute of Geology), St. Petersburg, (1997).

Blisniuk, K., Oskin, M., Fletcher, K., Rockwell, T., Sharp, W., 2012. Assessing the reliability of U-series and ^{10}Be dating techniques on alluvial fans in the Anza Borrego Desert, California. Quaternary Geochronology 13, 26–41.

Bowman, D., Korjenkov, A., Porat, N., Czassny, B., 2004. Morphological response to Quaternary deformation at an intermontane basin piedmont, the northern Tien Shan, Kyrgyzstan. Geomorphology 63, 1–24.

Brown, E.T., Bourlès, D.L., Burchfiel, B.C., Deng, Q.D., Li, J., Molnar, P., Raisbeck, G.M., Yiou, F., 1998. Estimation of slip rates in the southern Tien Shan using cosmic ray exposure dates of abandoned alluvial fans. Geological Society of America Bulletin 110, 377–386.

Bullen, M.E., Burbank, D.W., Garver, J.I., Abdrakhmatov, K.Y., 2001. Late Cenozoic tectonic evolution of the northwestern Tien Shan: new age estimates for the initiation of mountain building. Geological Society of America Bulletin 113, 1544–1559.

Bullen, M.E., Burbank, D.W., Garver, J.I., 2003. Building the Northern Tien Shan: integrated thermal, structural, and topographic constraints. Journal of Geology 111, 149–165.

Burchfiel, B.C., Brown, E.T., Deng, Q.D., Feng, X.Y., Li, J., Molnar, P., Shi, J.B., Wu, Z.M., You, H.C., 1999. Crustal shortening on the margins of the Tien Shan, Xinjiang, China. International Geology Review 41, 665–700.

Charreau, J., Avouac, J.P., Chen, Y., Dominguez, S., Gilder, S., 2008. Miocene to present kinematics of fault-bend folding across the Huerguosi anticline, northern Tianshan (China), derived from structural, seismic, and magnetostratigraphic data. Geology 36, 871–874.

Charreau, J., et al., 2009. Neogene uplift of the Tian Shan Mountains observed in the magnetic record of the Jingou River section (northwest China). Tectonics 28, TC2008. http://dx.doi.org/10.1029/2007TC002137.

Cheng, H., Zhang, P.Z., Spötl, C., Edwards, R.L., Cai, Y.J., Zhang, D.Z., Sang, W.C., Tan, M., An, Z.S., 2012. The climatic cyclicity in semiarid–arid central Asia over the past 500,000 years. Geophysical Research Letters 39, L01705. http://dx.doi.org/10.1029/2011GL050202.

Chmeleff, J., von Blanckenburg, F., Kossert, K., Jakob, D., 2010. Determination of the ^{10}Be half-life by multicollector ICP-MS and liquid scintillation counting. Nuclear Instruments and Methods in Physics Research Section B: Beam Interactions with Materials and Atoms 268, 192–199.

Daëron, M., Avouac, J.-P., Charreau, J., 2007. Modeling the shortening history of a fault tip fold using structural and geomorphic records of deformation. Journal of Geophysical Research 112, B03S13. http://dx.doi.org/10.1029/2006JB004460.

Desilets, D., Zreda, M., Prabu, T., 2006. Extended scaling factors for in situ cosmogenic nuclides: new measurements at low latitude. Earth and Planetary Science Letters 246, 265–276.

Dunai, T.J., 2001. Influence of secular variation of the geomagnetic field on production rates of in situ produced cosmogenic nuclides. Earth and Planetary Science Letters 193, 197–212.

Goethals, M.M., Hetzel, R., Niedermann, S., Wittmann, H., Fenton, C.R., Kubik, P.W., Christl, M., von Blanckenburg, F., 2009. An improved experimental determination of cosmogenic $^{10}Be/^{21}Ne$ and $^{26}Al/^{21}Ne$ production ratios in quartz. Earth and Planetary Science Letters 284, 187–198.

Gold, R.D., Cowgill, E., Arrowsmith, J.R., Chen, X., Sharp, W.D., Cooper, K.M., Wang, X.-F., 2011. Faulted terrace risers place new constraints on the late Quaternary slip rate for the central Altyn Tagh fault, northwest Tibet. Geological Society of America Bulletin 123, 958–978.

Gosse, J.C., Phillips, F.M., 2001. Terrestrial in situ cosmogenic nuclides: theory and application. Quaternary Science Reviews 20, 1475–1560.

Granger, D.E., Riebe, C.S., 2007. Cosmogenic nuclides in weathering and erosion. In: Holland, H.D., Turekian, K.K. (Eds.), Surface and ground water, weathering, and soils. Treatise on Geochemistry, 5, pp. 1–43.

Hancock, G.S., Anderson, R.S., Chadwick, O.A., Finkel, R.C., 1999. Dating fluvial terraces with ^{10}Be and ^{26}Al profiles: application to the Wind River, Wyoming. Geomorphology 27, 41–60.

Hein, A.S., Hulton, N.R.J., Dunai, T.J., Schnabel, C., Kaplan, M.R., Naylor, M., Xu, S., 2009. Middle Pleistocene glaciation in Patagonia dated by cosmogenic-nuclide measurements on outwash gravels. Earth and Planetary Science Letters 286, 184–197.

Heisinger, B., Lal, D., Jull, A.J.T., Kubik, P.W., Ivy-Ochs, S., Knie, K., Nolte, E., 2002a. Production of selected cosmogenic radionuclides by muons: 2. Capture of negative muons. Earth and Planetary Science Letters 200, 357–369.

Heisinger, B., Lal, D., Jull, A.J.T., Kubik, P.W., Ivy-Ochs, S., Neumaier, S., Knie, K., Lazarev, V., Nolte, E., 2002b. Production of selected cosmogenic radionuclides by muons 1. Fast muons. Earth and Planetary Science Letters 200, 345–355.

Hendrix, M.S., Graham, S.A., Carroll, A.R., Sobel, E.R., McKnight, C.L., Schulein, B.J., Wang, Z.X., 1992. Sedimentary record and climatic implications of recurrent deformation in the Tian Shan: evidence from Mesozoic strata of the north Tarim, south Junggar, and Turpan basins, northwest China. Geological Society of America Bulletin 104, 53–79.

Hendrix, M.S., Dumitru, T.A., Graham, S.A., 1994. Late Oligocene–Early Miocene unroofing in the Chinese Tian Shan: an early effect of the India–Asia collision. Geology 22, 487–490.

Hetzel, R., 2013. Active faulting, mountain growth, and erosion at the margins of the Tibetan Plateau constrained by in situ-produced cosmogenic nuclides. Tectonophysics 582, 1–24.

Hetzel, R., Tao, M., Stokes, S., Niedermann, S., Ivy-Ochs, S., Gao, B., Strecker, M.R., Kubik, P.W., 2004. Late Pleistocene/Holocene slip rate of the Zhangye thrust (Qilian Shan, China) and implications for the active growth of the northeastern Tibetan Plateau. Tectonics 23, TC6006. http://dx.doi.org/10.1029/2004TC001653.

Hidy, A.J., Gosse, J.C., Pederson, J.L., Mattern, J.P., Finkel, R.C., 2010. A geologically constrained Monte Carlo approach to modeling exposure ages from profiles of cosmogenic nuclides: an example from Lees Ferry, Arizona. Geochemistry, Geophysics, Geosystems 11, Q0AA10. http://dx.doi.org/10.1029/2010GC003084.

Hubert-Ferrari, A., Suppe, J., Van Der Woerd, J., Wang, X., Lu, H., 2005. Irregular earthquake cycle along the southern Tianshan front, Aksu area, China. Journal of Geophysical Research 110, B06402. http://dx.doi.org/10.1029/2003JB002603.

Jolivet, M., Dominguez, S., Charreau, J., Chen, Y., Li, Y.G., Wang, Q.C., 2010. Mesozoic and Cenozoic tectonic history of the central Chinese Tian Shan: reactivated tectonic structures and active deformation. Tectonics 29, TC6019. http://dx.doi.org/10.1029/2010TC002712.

Kirby, E., Harkins, N., Wang, E., Shi, X., Fan, C., Burbank, D., 2007. Slip rate gradients along the eastern Kunlun fault. Tectonics 26, TC2010. http://dx.doi.org/10.1029/2006TC002033.

Kober, M., Seib, N., Kley, J., Voigt, T., 2013. Thick-skinned thrusting in the northern Tien Shan foreland, Kazakhstan: structural inheritance and polyphase deformation. In: Nemcok, M., Mora, A., Cosgrove, J.W. (Eds.), Thick-skin-dominated orogens: from initial inversion to full accretion. Geological Society, London, Special Publications, 377. http://dx.doi.org/10.1144/SP377.7.

Kohl, C.P., Nishiizumi, K., 1992. Chemical isolation of quartz for measurement of in-situ-produced cosmogenic nuclides. Geochimica et Cosmochimica Acta 56, 3583–3587.

Korschinek, G., et al., 2010. A new value for the half-life of ^{10}Be by heavy-ion elastic recoil detection and liquid scintillation counting. Nuclear Instruments and Methods in Physics Research Section B: Beam Interactions with Materials and Atoms 268, 187–191.

Kubik, P.W., Christl, M., 2010. ^{10}Be and ^{26}Al measurements at the Zurich 6 MV Tandem AMS facility. Nuclear Instruments and Methods in Physics Research Section B: Beam Interactions with Materials and Atoms 268, 880–883.

Lal, D., 1991. Cosmic ray labeling of erosion surfaces: in situ nuclide production rates and erosion models. Earth and Planetary Science Letters 104, 424–439.

Li, C.X., Guo, Z.J., Dupont-Nivet, G., 2011. Late Cenozoic tectonic deformation across the northern foreland of the Chinese Tian Shan. Journal of Asian Earth Sciences 42, 1066–1073.

Lifton, N.A., Bieber, J.W., Clem, J.M., Duldig, M.L., Evenson, P., Humble, J.E., Pyle, R., 2005. Addressing solar modulation and long-term uncertainties in scaling secondary cosmic rays for in situ cosmogenic nuclide applications. Earth and Planetary Science Letters 239, 140–161.

Matmon, A., Nichols, K., Finkel, R., 2006. Isotopic insights into smoothening of abandoned fan surfaces, southern California. Quaternary Research 66, 109–118.

Nishiizumi, K., Imamura, M., Caffee, M.W., Southon, J.R., Finkel, R.C., McAninch, J., 2007. Absolute calibration of ^{10}Be AMS standards. Nuclear Instruments and Methods in Physics Research Section B: Beam Interactions with Materials and Atoms 258, 403–413.

Palumbo, L., Hetzel, R., Tao, M., Li, X., Guo, J., 2009. Deciphering the rate of mountain growth during topographic pre-steady state: an example from the NE margin of the Tibetan Plateau. Tectonics 28, TC4017. http://dx.doi.org/10.1029/2009TC002455.

Perg, L.A., Anderson, R.S., Finkel, R.C., 2001. Use of a new ^{10}Be and ^{26}Al inventory method to date marine terraces, Santa Cruz, California, USA. Geology 29, 879–882.

Petrov, O.V.; Leonov, Yu.G.; Tingdong, L.; Tomurtogoo, O.; Shokalsky, S.P.; Pospelov, I.I.; Bingwei, C.; Koshkin, V.Ya.; Jae Hae, H. (editors), Tectonic map of Central Asia and adjacent areas, scale 1:2.500.000, Commission de la Carte Géologique du Monde/Commission for the Geological Map of the World, Paris, (2007).

Reigber, C., Michel, G.W., Galas, R., Angermann, D., Klotz, J., Chen, J.Y., Papschev, A., Arslanov, R., Tzurkov, V.E., Ishanov, M.C., 2001. New space geodetic constraints on the distribution of deformation in Central Asia. Earth and Planetary Science Letters 191, 157–165.

Ritz, J.F., et al., 2003. Late Pleistocene to Holocene slip rates for the Gurvan Bulag thrust fault (Gobi-Altay, Mongolia) estimated with ^{10}Be dates. Journal of Geophysical Research 108, 2162. http://dx.doi.org/10.1029/2001JB000553.

Scharer, K.M., Burbank, D.W., Chen, J., Weldon, R.J., Rubin, C., Zhao, R., Shen, J., 2004. Detachment folding in the southwestern Tien Shan–Tarim foreland, China: shortening estimates and rates. Journal of Structural Geology 26, 2119–2137.

Schmidt, S., Hetzel, R., Kuhlmann, J., Mingorance, F., Ramos, V.A., 2011. A note of caution on the use of boulders for exposure dating of depositional surfaces. Earth and Planetary Science Letters 302, 60–70.

Selander, J., Oskin, M., Ormukov, C., Abdrakhmatov, K., 2012. Inherited strike-slip faults as an origin for basement-cored uplifts: example of the Kungey and Zailiskey ranges, northern Tian Shan. Tectonics 31, TC4026. http://dx.doi.org/10.1029/2011TC003002.

Siame, L., et al., 2004. Local erosion rates versus active tectonics: cosmic ray exposure modelling in Provence (south-east France). Earth and Planetary Science Letters 220, 345–364.

Sobel, E.R., Dumitru, T.A., 1997. Thrusting and exhumation around the margins of the western Tarim basin during the India–Asia collision. Journal of Geophysical Research 102, 5043–5063.

Sobel, E.R., Chen, J., Heermance, R.V., 2006. Late Oligocene–Early Miocene initiation of shortening in the Southwestern Chinese Tian Shan: implications for Neogene shortening rate variations. Earth and Planetary Science Letters 247, 70–81.

Stone, J.O., 2000. Air pressure and cosmogenic isotope production. Journal of Geophysical Research 105, 23753–23759.

Tapponnier, P., Molnar, P., 1979. Active faulting and Cenozoic tectonics of the Tien Shan, Mongolia, and Baykal regions. Journal of Geophysical Research 84, 3425–3459.

Thompson, S.C., Weldon, R.J., Rubin, C.M., Abdrakhmatov, K.Y., Molnar, P., Berger, G.W., 2002. Late Quaternary slip rates across the central Tien Shan, Kyrgyzstan, central Asia. Journal of Geophysical Research 107, 2203. http://dx.doi.org/10.1029/2001JB000596.

Windley, B.F., Allen, M.B., Zhang, C., Zhao, Z.Y., Wang, G.R., 1990. Paleozoic accretion and Cenozoic redeformation of the Chinese Tien Shan Range, central Asia. Geology 18, 128–131.

Windley, B.F., Alexeiev, D., Xiao, W., Kröner, A., Badarch, G., 2007. Tectonic models for accretion of the Central Asian Orogenic Belt. Journal of the Geological Society (London) 164, 31–47.

Yang, S., Li, J., Wang, Q., 2008. The deformation pattern and fault rate in the Tianshan Mountains inferred from GPS observations. Science in China Series D: Earth Sciences 51, 1064–1080.

Yin, A., 2010. Cenozoic tectonic evolution of Asia: a preliminary synthesis. Tectonophysics 488, 293–325.

Yin, A., Nie, S., Craig, P., Harrison, T.M., Ryerson, F.J., Qian, X., Yang, G., 1998. Late Cenozoic tectonic evolution of the southern Chinese Tian Shan. Tectonics 17, 1–27. http://dx.doi.org/10.1029/97TC03140.

Zechar, J.D., Frankel, K.L., 2009. Incorporating and reporting uncertainties in fault slip rates. Journal of Geophysical Research 114, B12407. http://dx.doi.org/10.1029/2009JB006325.

Zehfuss, P.H., Bierman, P.R., Gillespie, A.R., Burke, R.M., Caffee, M.W., 2001. Slip rates on the Fish Springs fault, Owens Valley, California, deduced from cosmogenic ^{10}Be and ^{26}Al and soil development on fan surfaces. Geological Society of America Bulletin 113, 241–255.

Zubovich, A.V., et al., 2010. GPS velocity field for the Tien Shan and surrounding regions. Tectonics 29, TC6014. http://dx.doi.org/10.1029/2010TC002772.